Magnetic Resonance in Medicine 000:000–000 (2011)

Ultrashort Echo Time Imaging Using Pointwise Encoding Time Reduction With Radial Acquisition (PETRA)

David M. Grodzki,[1,2]* Peter M. Jakob,[1] and Bjoern Heismann[2,3]

Sequences with ultrashort echo times enable new applications of MRI, including bone, tendon, ligament, and dental imaging. In this article, a sequence is presented that achieves the shortest possible encoding time for each *k*-space point, limited by pulse length, hardware switching times, and gradient performance of the scanner. In pointwise encoding time reduction with radial acquisition (PETRA), outer *k*-space is filled with radial half-projections, whereas the centre is measured single pointwise on a Cartesian trajectory. This hybrid sequence combines the features of single point imaging with radial projection imaging. No hardware changes are required. Using this method, 3D images with an isotropic resolution of 1 mm can be obtained in less than 3 minutes. The differences between PETRA and the ultrashort echo time (UTE) sequence are evaluated by simulation and phantom measurements. Advantages of pointwise encoding time reduction with radial acquisition are shown for tissue with a T_2 below 1 ms. The signal to noise ratio and Contrast-to-noise ratio (CNR) performance, as well as possible limitations of the approach, are investigated. In-vivo head, knee, ankle, and wrist examples are presented to prove the feasibility of the sequence. In summary, fast imaging with ultrashort echo time is enabled by PETRA and may help to establish new routine clinical applications of ultrashort echo time sequences. Magn Reson Med 000:000–000, 2011. © 2011 Wiley-Liss, Inc.

Key words: Ultrashort echo time; radial acquisition; single point sequence

In MR experiments, the transversal magnetization decays with T_2^*. Standard MR sequences offer echo times (TEs) in the range of a few milliseconds for spin-echo sequences and down to 1 ms for gradient-echo sequences. Signals arising from tissues with a very short T_2, well below 1 ms, are therefore not visible using standard sequences, as the signal has already decayed by the time of acquisition. In the image, these tissues appear dark, similar to air cavities or noise. A short T_2 can usually be found in tissue with strong couplings of solid materials like teeth, ligaments, tendons, and bones in the human body.

Many regions of the human body have already been investigated with ultrashort echo time sequences. Clinical applications of sequences with ultrashort TE are used in orthopedics, dental imaging, and many other special applications. Studies not only of the knee (1), Achilles tendon (2,3), brain (4), bone (5) and spine (6) but also of the lungs (7) can be found in the literature.

Ultrashort TE sequences also have a couple of other features. Dephasing of spins between excitation and acquisition is much smaller than for conventional sequences. Ultrashort TE-sequences are therefore able to image tissue close to magnetic inhomogeneities or distortions. These distortions may arise from susceptibility changes, e.g., in close proximity to air cavities, prostheses, or magnet and gradient imperfections. Little or no susceptibility artefacts can be expected in ultrashort TE images compared to standard gradient-echo or spin-echo sequences. Therefore, ultrashort TE sequences can also be used for positive contrast imaging of iron-labeled capsules (8,9). Furthermore, ultrashort TE sequences offer new possibilities for imaging other nuclei than hydrogen. These nuclei often have strong bonds to their neighbors and therefore have a very short T_2. In (10) and (11), sodium and phosphorus images were acquired.

In addition, obtaining a bone signal enables segmentation of images into soft tissue (water), bone, and air (12). This allows calculation of so-called μ-maps, which are needed for combined MR and positron emission tomography (PET) images. For PET imaging, the attenuation of tissue has to be included into image reconstruction with the so-called attenuation correction.

Imaging tissue with short T_2 has challenging demands on MR hardware. As signal already starts to decay exponentially with T_2 at the center of the pulse, data acquisition should begin as quickly as possible after excitation. The dead time between transmission and receive in operation is limited by ringing down of the coil with stored RF energy after transmission and retuning the receive coil before acquisition. For most clinical scanners, this time is in the range of 40 to 100 μs. With some hardware changes, dead times down to 8 μs have been reported on clinical scanners (13).

In the last decade, dedicated sequences with ultrashort echo times have been developed. Most of them either use Cartesian single point acquisition or radial acquisition of *k*-space.

Single point sequences like the Rapid Single Point (RASP) or Single-Point Ramped Imaging with T_1 Enhancement (SPRITE) sequence use a straightforward approach (14–16). Cartesian *k*-space values are filled up point by point, using only one or a few (17,18) points per readout for image calculation at a constant encoding time. Single point sequences use short hard pulses, which are applied after ramping up the gradients. In this case, the encoding time equals the TE. The minimum encoding time is given by

---

[1] Department of Experimental Physics 5, University of Wuerzbug, Wuerzbug, Germany
[2] Magnetic Resonance, Siemens AG, Erlangen, Germany
[3] Friedrich-Alexander-University Erlangen-Nuremberg, Erlangen, Germany

*Correspondence to: David Grodzki, Diploma in Physics, Healthcare Sector, Siemens AG, Allee am Roethelheimpark 2, D-91052 Erlangen, Germany. E-mail: david.grodzki.ext@siemens.com

Received 29 September 2010; revised 28 April 2011; accepted 29 April 2011.
DOI 10.1002/mrm.23017

the resolution and available gradient strengths. For clinical whole body scanners, the encoding time is often too long for imaging tissue with very short T_2 at a reasonable resolution. A workaround has been proposed that uses the shortest encoding time available for every single k-space point and enables significantly shorter TEs (19). Although good signal to noise ratio (SNR) and image quality can be achieved with single point sequences, measurement times are very long and prevent application of single point methods in most clinical circumstances.

The most common method for imaging tissue with ultrashort T_2 is the so called Ultrashort Echo Time (UTE) sequence (20–22). Once the dead time after excitation is passed, gradient ramp-up and data acquisition are started simultaneously. k-Space is filled up on radial trajectories. This leads to a higher point density at k-space centre, which has to be taken into account during image reconstruction. k-Space points are regridded onto Cartesian points. One challenge of the UTE sequence is that acquiring data during gradient ramping can lead to major image distortions originating from eddy currents and time delays within the gradient system.

Projection imaging or zero-TE imaging overcomes this problem. Gradients are ramped up before a hard excitation pulse is applied (23,24). Data acquisition is started after the dead time has passed. This leads to a gap at the centre of k-space, as the k-space value to be acquired begins to rise from the center of the pulse. Two methods have been proposed to solve this problem. In one approach, the missing k-space points are filled up by algebraic reconstruction (25). In the other approach (26,27), after the end of the measurement a few more radial spokes are acquired using lower gradient strength, so that at least parts of the gap can be filled with measured data. Projection imaging offers very short measurement times. A potential drawback of these methods is that only 3D imaging is possible, while UTE offers slice-selective pulses to be applied for 2D imaging.

Hard and very short pulses only allow limited flip angles due to limited pulse duration and available maximum B_1 amplitude. If gradients are already on when the pulse is applied, further limitation in bandwidth and duration of the pulse may occur. Sweep imaging with Fourier transformation (SWIFT) splits the applied pulse in N subpulses (28). A subadiabatic frequency sweep is performed. Higher effective flip angles are possible. To reach higher SNR compared to hard-pulsed sequences, almost no dead time is needed (29).

In this study, we propose a new method combining radial and Cartesian single point acquisition. The radial part of the sequence is similar to projection imaging sequences, while the gap in the middle of k-space is filled on a Cartesian trajectory comparable to single point sequences. By this, the gap in the middle of k-space is completely filled with exact values. Our approach ensures that every single k-space point is measured with the smallest encoding time available on the scanner. During image reconstruction, both datasets are combined.

METHODS

Imaging Sequence

The PETRA sequence consists of a radial and a Cartesian acquisition part. Like in key-hole imaging (30), outer and inner k-space are acquired in two parts. A low resolution image is aquired in the Cartesian part, and high spatial frequency data are acquired in the radial part of the sequence. The radial part of the sequence runs similar to projection imaging methods. Radial spokes are evenly distributed over a sphere in k-space as described in (31) with the trajectory used in (10). After the gradient ramp-up, a hard low-flip angle pulse is applied and readout is started at the echo time $t = \text{TE}$. Figure 1 illustrates the sequence diagram. The applied absolute gradient strength $|\vec{G}| = \sqrt{G_x^2 + G_y^2 + G_z^2}$ is kept constant during the radial part. As encoding of spins starts at $t = 0$ at the middle of the pulse, the point in k-space acquired at TE is given by

$$\vec{k}^* = \gamma \vec{G}\,\text{TE}. \qquad [1]$$

k-Space values with $|k| < |\vec{k}^*|$ cannot be measured in this way, because they would have to be measured before the dead time has passed. These missing points in the middle of k-space are essential for image reconstruction to reach high SNRs. In our approach, these points are filled up pointwise in the Cartesian part of the sequence. Every Cartesian k-space value that lies within the sphere of $|\vec{k}| < |\vec{k}^*|$ is measured, see Fig. 1c. The Cartesian measurement runs similar to single point sequences as described in Refs. 15,16, and 19. Gradients are ramped up before the pulse is applied, like in the radial part of the sequence, and one single point is acquired at $t = \text{TE}$. To measure a certain k-space point $\vec{k}$ with $|\vec{k}| \le |\vec{k}^*|$, the gradient strength in each spatial direction is given by

$$\vec{G} = \frac{\vec{k}}{\gamma \text{TE}}, \qquad [2]$$

e.g., all gradients are zero for $\vec{k} \equiv 0$ and a Free Induction Decay (FID) signal is acquired at $t = \text{TE}$.

While $|\vec{G}|$ is kept constant in the radial part, the encoding time is kept constant in the Cartesian part. Equations 1 and 2 imply that the applied gradient strength in the Cartesian part of the sequence is always lower than the gradient strength used during the radial part of the sequence. In our implementation, only one k-space point is acquired at each Cartesian readout.

As gradients are switched on during excitation, PETRA can only be used as a 3D method with nonselective excitations. In the current implementation, isotropic 3D data is collected.

PETRA acquisition time is a bit longer than projection imaging time due to the time needed for the Cartesian acquisition. As an example, for an applied gradient strength of 20 mT/m and a resolution of 1 mm, the time needed to encode the outer edge of k-space would be $T_{\text{enc}} \approx 600\,\mu\text{s}$. Considering an echo time of $\text{TE} = 50\,\mu\text{s}$, this means that $50/600 = 8\%$ of k-space needs to be acquired using Cartesian points. For an $N = 256^3$ matrix, the number of Cartesian points is therefore $N_{\text{cart}} = 4/3\pi(256/2 \times 0.08)^3 \approx 4450$. Compared to, e.g., 50,000 radial spokes, this is less than 9%. Hence, measurement time of PETRA is about 5–10% longer than that for projection imaging.

TE can basically be set to any value bigger than the dead time plus half of the pulse duration. For longer TEs, only

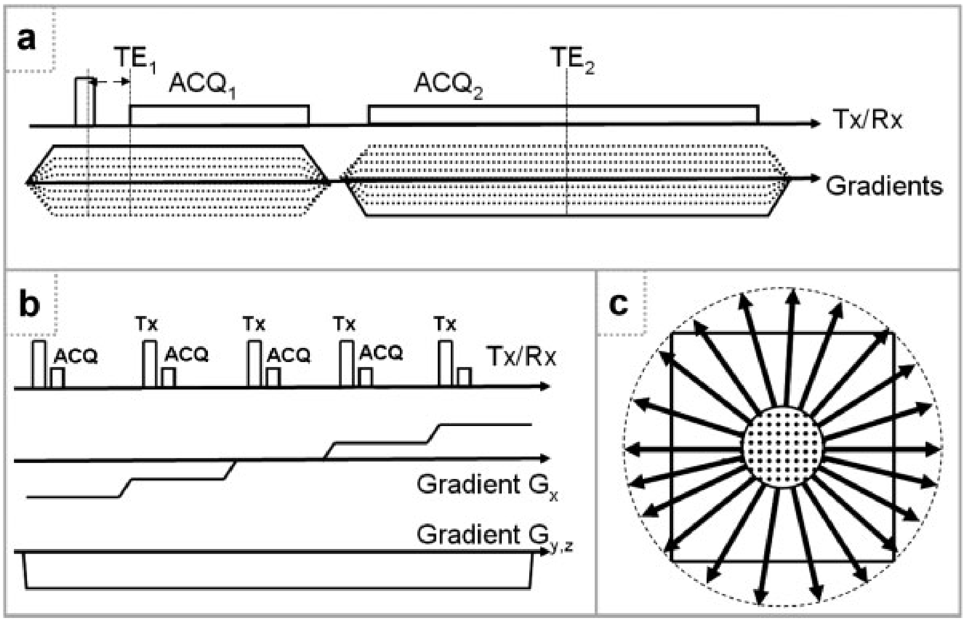

FIG. 1. **a**: Diagram of the radial part of the PETRA sequence. After a hard-pulse excitation, a radial half-projection is acquired. In case of a second echo generation, gradients are ramped down at the end of the first acquisition and a second full-projection with the echo time TE_2 is acquired. **b**: Diagram of the Cartesian part of the sequence. Gradients are stepped through to cover all missing *k*-space points in the centre. **c**: PETRA *k*-space acquisition schema plotted for one slice through the middle of the 3D *k*-space data.

the ratio between *k*-space points acquired radially or on the Cartesian trajectory changes. This flexibility enables T_2^* quantification, as image series with different TEs can be measured and evaluated.

When fat saturation is desired, fat saturation pulses were added to the PETRA sequence. During the application of the saturation pulse, gradients are switched off. Before the imaging pulse is applied, gradients are ramped up again. Depending on selected repetition time TR, a fat suppression pulse was inserted only at every *n*th run, $n \approx 5 - 20$. Repetition time (TR) is not changed if fat saturation is selected.

If TR and the flip angle α are kept constant, spins are forced into a steady state. If saturation pulses are applied, the steady state is interrupted by the duration of the saturation. The steady state influences the contrast of the image. At the end of each repetition, spins have to be completely spoiled. The contrast resembles FLASH contrast and ranges from proton-density to T_1 contrast, depending on TR and the flip angle. For a given tissue with proton density ϱ, signal S arising from this tissue can be approximated by the Ernst equation for short TE

$$S = \varrho \sin(\alpha) \frac{1 - \exp(-\mathrm{TR}/T_1)}{1 - \cos(\alpha)\exp(-\mathrm{TR}/T_1)}. \qquad [3]$$

To obtain an image that only contains signal from tissue with short T_2, two methods have been proposed. T_2-selective prepulses can be used just to suppress tissue with longer T_2 (32–36). The other possibility is to reverse the gradient polarity after the readout and refocus the spin system to a second echo at a second echo time TE_2. With this method, two images are produced in one measurement. These two images can be subtracted, leaving only signal from tissue with a short T_2. In (37), the subtraction method is presented to be the more reliable alternative. In our implementation, a second echo can be acquired with the PETRA sequence. As it can be seen in Fig. 1a, gradients are inverted once the first half-projection is acquired and spins are refocused to a gradient echo at $t = \mathrm{TE}_2$. During the second readout, a full projection is acquired. It is possible to reconstruct the second echo with data acquired only from radial spokes, as no gap arises in the *k*-space of the second echo.

Image Reconstruction

Image reconstruction was performed with the image calculation environment of a MAGNETOM Avanto (SIEMENS Healthcare, Erlangen, Germany). The *k*-space has to be filled up on a Cartesian grid. While the points acquired in the Cartesian part of the sequence can simply be gridded to their corresponding position, data handling for the radial part is more complex. Before the radial spokes are gridded onto the Cartesian grid, their values have to be weighted with a density matrix (38). Two more facts have to be considered. First, it needs to be ensured that the density matrix is adapted to the density of points in the Cartesian centre of *k*-space. Second, if not enough radial spokes are acquired and *k*-space is radially undersampled, a certain level of plateau of the outer part of the density matrix can improve image quality at the expense of image resolution. In our implementation, we use a density matrix that adapts these needs to the methods described in (39).

According to the Nyquist criterion, the total amount of radial spokes N_{Spokes} needed is given by $N_{\mathrm{Spokes}} = 4\pi R^2$ (10), where R is the number of points acquired for each radial half-projection. A matrix size of $N = 256$ in which

$R = 128$ points are acquired at every half-projection would therefore need $N_{\mathrm{Spokes}} \approx 200{,}000$ radial spokes. In our measurements, we only use a number of $N_{\mathrm{Spokes}} \leq 50{,}000$. The level of plateau of the density matrix is reached at point R_{Pl} of the readout.

After the density matrices are applied to the radially sampled data, points are gridded onto the Cartesian grid using a Kaiser-Bessel-Window (40) with a width of 3.0 and $\beta = 4.2054$, which was used in Ref. 10. For multi-receive channel imaging, a weighted root-sum-of-squares algorithm is used for image reconstruction.

MR Simulations

The impact of the T_2 decay on the optimal performance of UTE and PETRA sequences was investigated by simulation using MATLAB 2008 (The MathWorks Inc., Natick, MA). A 1D object as shown in Fig. 3 with a given T_2 between 50 and 1000 μs was considered. The object was Fourier-transformed to calculate the corresponding 1D k-space. Each k-space value k_i was multiplied with the factor $f = \exp(-T_{\mathrm{Enc},i}/T_2)$, where $T_{\mathrm{Enc},i}$ corresponds to the encoding time needed to encode the k-space value for the UTE and PETRA sequence, respectively. The factor f corresponds to the T_2 decay a spin experiences in a MR experiment using the two sequences. An inverse Fourier transformation yields the UTE and PETRA image. Simulation conditions were TE = 50 μs, gradient strength 20 mT/m, slewrate 100 mT (m ms), field of view (FOV) = 200 mm, and a matrix size of $N = 256$. The modulation transfer function (MTF) (41) was calculated for a delta-shaped object. The MTF distinguishes image resolution quantitatively.

MR Measurements

MR measurements were performed on a 1.5 T MAGNETOM Avanto clinical scanner. The scanner and coil hardware was not adapted. When a second echo was acquired, its echo time was set to $\mathrm{TE}_2 = 4.6$ ms to reach an in-phase fat signal. Repetition time was set to 2–5 ms for single-echo series and to 6–10 ms for series with two echoes. Using a total of 50,000 spokes, total measurement time for both radial and Cartesian part of the sequences was in the range of 2–4 min for single echo series and 5–10 min for a series with two echos. No radiofrequency (RF) spoiling was used. The maximum gradient strength was set to 8–15 mT/m in each spatial direction with a typical ramp time of 0.5–1 ms.

A standard four-channel head coil, a standard 15-channel transmission/receive knee coil, a standard eight-channel wrist coil and a standard eight-channel ankle coil were used. The used head, wrist, and ankle coil are recieve-only coils. For those coils, the body coil was used for transmission. The dead time of the coils is in the range of 50 μs. Rectangular hard pulses with a duration of about 14 μs and flip angles up to 9° were used for excitation. TE was set to $\mathrm{TE}_1 = 70$ μs for the head and ankle coil and to $\mathrm{TE}_1 = 50$ μs for the wrist and knee coil.

Phantom measurements were performed on bovine marrowbone (cortical bone). Different amounts of radial spokes have been tested to detect the dependency on the total number of spokes and level of plateau of the radial density matrix. A comparison measurement between UTE and PETRA was conducted. The UTE sequence was implemented according to (10). For this measurement, the following parameters were used: 1.3 mm resolution with a 192^3 matrix, 50,000 radial spokes, $\alpha = 8°$, head coil, readout gradient strengths 12 mT/m, and TE = 70 μs. To have identical steady-state contrasts, TR in both sequences was set to TR = 2.83 ms, which was the minimum TR for UTE. PETRA would allow for a TR of 2.21 ms in this case.

In vivo experiments of the wrist, knee, ankle, and head were performed on healthy volunteers after informed consent was attained. Also, PETRA was tested on a knee of one of the authors, whose anterior cruciate ligament was reformed after rupture 4 months prior to imaging. In both the phantom and in vivo experiments as well as for series with one and two echos, the sequence was tested with and without additional gradient spoiling at the end of each repetition.

Finally, possible limitation and artefacts in PETRA imaging originating from the excitation profile were investigated. As gradients are kept on during the pulse, unwanted slice selectivity may occur for insufficient pulse bandwidths. The spectral profile of the 14 μs pulse is a sinc curve with a full width at half maximum of about 86 kHz. If this bandwidth is not sufficient for a given gradient strength, higher frequencies might not be excited homogeneously. Gradients are altered for each repetition so that different slices would be excited at each repetition. To investigate this possible limitation, images with large FOVs were acquired with gradient strengths from 2 to 18 mT/m.

RESULTS

In Fig. 2, the time needed for k-space encoding of UTE and PETRA are shown. PETRA has shorter encoding times over the whole k-space. This is due to the fact, that no encoding time is lost during gradient ramp-ups. k-Space points with an absolute value smaller than k^* have the constant encoding time TE at PETRA. For values $|k| > k^*$, the needed encoding time rises linearly. In UTE imaging, the encoding time rises quadratically during gradient ramping and linearly once gradient ramping is over.

In the presence of chemical shifts or B_0 inhomogeneities, phase shifts cause minor radial shifts in the image. These effects are similar to those known from the UTE sequence or projection methods. Unlike in the RASP or SPRITE sequence, PETRA has a nonconstant off-resonance evolution. For experimental data, we have observed no discontinuity in the development of phases also in the presence chemical shifts or B_0 inhomogeneities. This is due to the fact that there is no discontinuity in the encoding times over k-space, see Fig. 2. No further artefacts were observed due to the combination of the radial and Cartesian part of the sequence.

The simulation of a 1D object with different T_2 for UTE and PETRA is shown in Fig. 3. In the upper row, major differences for PETRA and UTE can be seen. The SNR of PETRA in comparison to UTE is about 53% higher for $T_2 = 100$ μs, 19% higher for $T_2 = 250$ μs and 6% higher for $T_2 = 750$ μs. Image resolution is clearly better with PETRA for very short T_2 tissue, which can be seen in the 1D object as well as in the MTF curves displayed in the lower row of

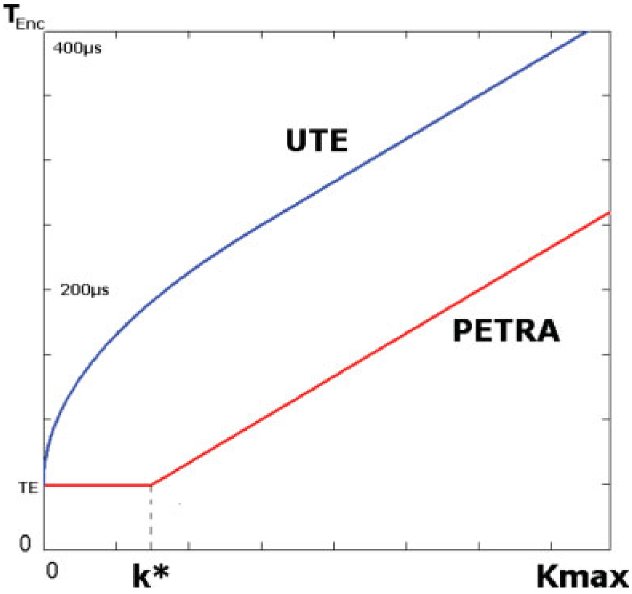

FIG. 2. Comparison of encoding times T_{Enc} depending on the point in k-space. While the encoding time for the UTE sequence rises quadratically during gradient ramping, PETRA's encoding time stays constant for $|k| < k^*$, see Eq. 1. T_{Enc} equals the TE. Afterward, PETRA's encoding time rises linearly. k-Space points with $|k| \leq k^*$ are acquired on a Cartesian trajectory, while k-space points with $|k| > k^*$ are acquired radially. PETRA enables lower encoding times for each acquired k-space point than the UTE sequence.

Fig. 3. For a T_2 longer than 1 ms, no major differences were found between UTE and PETRA.

In the phantom measurements, changing the level of plateau of the density matrix for the radial spokes leads to more noise, but better resolution for $R_{\mathrm{Pl}} > R/4$. For $R_{\mathrm{Pl}} < R/4$, lower noise but a reduced image resolution can be detected. An optimum between resolution and level of noise is found for $R_{\mathrm{Pl}} = \sqrt{1/2 \times N_{\mathrm{Spokes}}/\pi}$. Figure 4 shows the UTE (a) and PETRA (b) image acquired in comparison. The SNR of signal arising from cortical bone is in the range of 6.5 for UTE and 11.1 for PETRA, while SNR of surrounding tissue is in the range of 15 for UTE and 19 for PETRA. CNR between bone and air lies in the range of 14.0 for UTE and 19.1 for PETRA. Between bone and soft tissue, a CNR of about 21.1 for UTE and 15.3 for PETRA is found.

For series with one echo, it was found that the spoiling during the incremental gradient changes is sufficient and no additional gradient spoiling is needed at the end of each repetition. No differences between images with and without gradient spoiling were observed. It is not required to ramp down gradients at the end of each repetition and more beneficial to directly ramp the gradients to the strength needed for the next excitation and readout. The sequence then has almost no nerve stimulation and allows for very short TR. For series with two echos, gradient spoiling is needed at the end of each repetition to prevent the occurrence of unwanted echos.

The investigation of artefacts and limitations originating from the pulse profile showed no visible influences in the images at a FOV of 300 mm for gradient strengths lower than 12 mT/m. Using higher gradient strengths, blurring

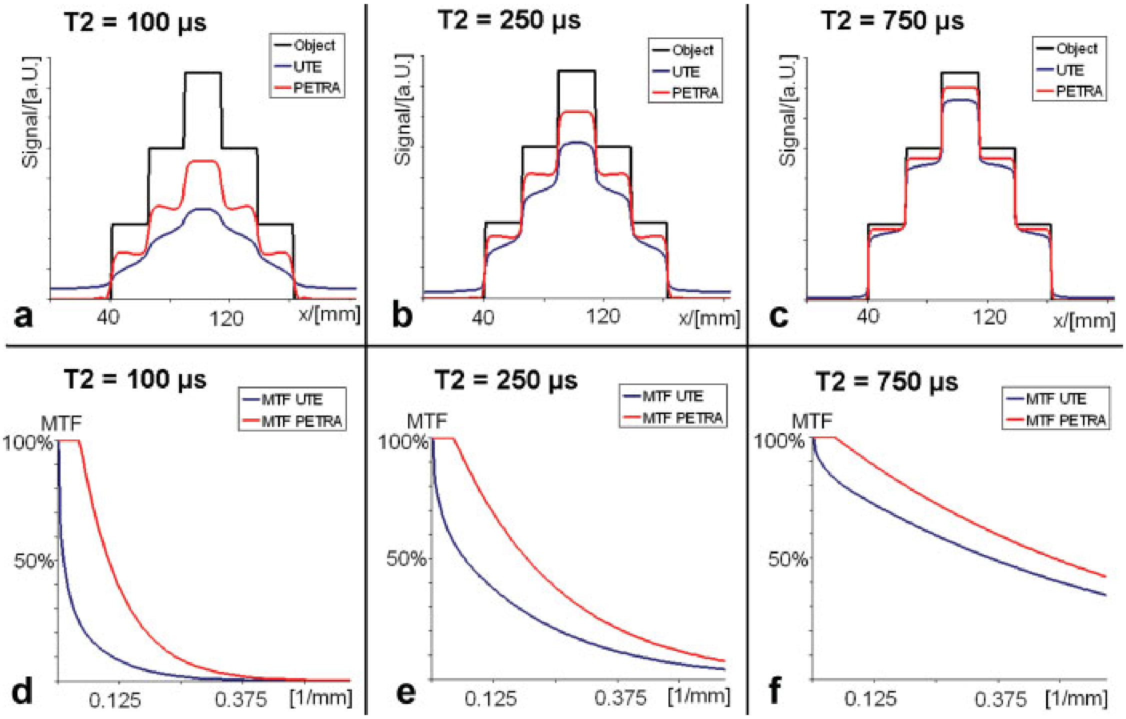

FIG. 3. Simulation of the influence of the T_2 decay for the UTE and PETRA sequence for the $T_2 = 100\,\mu\mathrm{s}$ in (**a**) and (**d**), $T_2 = 250\,\mu\mathrm{s}$ in (**b**) and (**e**) and $T_2 = 750\,\mu\mathrm{s}$ in (**c**) and (**f**). In the upper row, a 1D object with the length of 200 mm was simulated and the expected images for UTE and PETRA are calculated. In the lower row, the corresponding modulation transfer function (MTF) is presented.

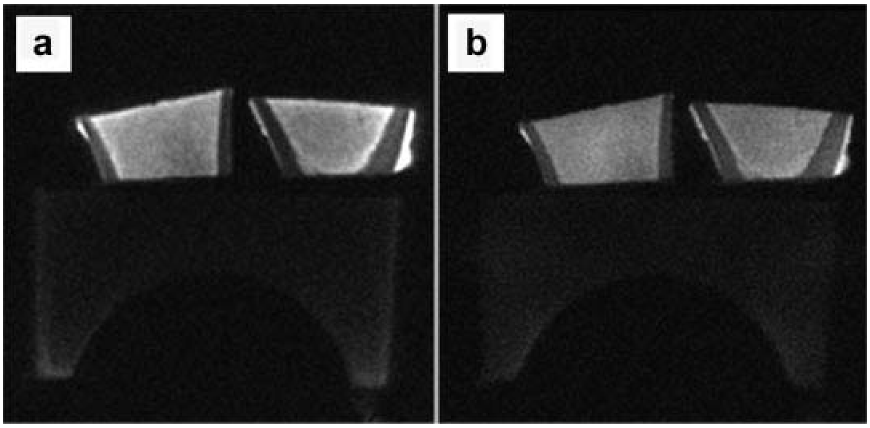

FIG. 4. Comparison measurement between UTE (**a**) and PETRA (**b**). Images are normalized to flesh signal and have identical windowing. Scanning parameters were 1.3 mm resolution with a 192^3 matrix, 50,000 radial spokes, $\alpha = 8°$, readout gradient strengths 12 mT/m, TE = 70 μs and TR = 2.83 ms. Measurement time was 2 min 22′ for UTE and 2 min 30′ for PETRA. The difference of 8 s was needed for the Cartesian part of the PETRA sequence.

artefacts are encountered at the outer regions of the image. For a FOV lower than 200 mm, no artefacts were found.

Figure 5 shows an image series of the head. Figure 5a and b shows the same slice without and with fat suppression. Figure 5c shows a head image with higher resolution in a coronal image plane. In these images, a homogeneous T_1 contrast is observed. Figure 5d, e and f shows an image series with two echos and the subtraction of the two echos. It is clearly visible that air within the paranasal sinuses yields no signal, while signal is obtained from the skull and bones. For longer TEs, these areas are dark, see Fig. 5e. This is highlighted in the subtraction image (Fig. 5f). Comparison of Fig. 5a and b shows that the fat suppression works well: retrobulbar fat behind the eyes and fat within the calvarium is bright in Fig. 5a, while this fat is saturated in Fig. 5b.

Wrist, ankle, and knee images show the same homogeneity as that found in the head images. Figure 6 displays a coronal slice of a series with two echos and the corresponding difference image of the human wrist. In Fig. 6a, strong signal can be seen from hand ligaments, while in Fig. 6b, at an TE of 4.6 ms, this signal is already decayed. Figure 6c highlights this fact and enables easy detection of hand ligaments and bones.

A subtraction image of the ankle is presented in Fig. 7. Comparable to the wrist image, bones, tendons, and ligaments appear bright and offer an easy detection of the foot bones as well as the Achilles tendon for excample. On the side of the ankle, signal from the coating of the coil is visible. Most coils, like for example the knee coil, give strong signal in PETRA images. In sequences with TE longer than about 750 μs, these bound protons within the coil coating are invisible due to their short T_2.

Figure 8 shows a sagittal MIP image of the knee, where the anterior cruciate ligament had been operated 4 months prior to measurement. The newly implanted anterior cruciate ligament (arrow 1) and its anchorage (arrow 3) in the bones can be seen. The newly implanted ligament is much stronger than the ligament of a healthy, unoperated knee or the posterior cruciate ligament (arrow 2). Noticeable susceptibility artefacts arising from metal screws and bolts used for fixing of the operated anterior cruciate ligament are very small in Fig. 8 (arrow 3).

DISCUSSION

A sequence with UTE was implemented that uses both radial and Cartesian acquisition. The feasibility of this technique was assessed in phantom and volunteer measurements on a 1.5 T clinical scanner. No artefacts generated by the combination of the two acquisitions are observed.

The conducted MR measurements in Figs. 4–8 prove PETRA's ability to image tissue with very short T_2. Good image quality can be achieved experimentally in fast imaging experiments. A reasonable resolution can be achieved even with a highly undersampled outer k-space.

Overall, the images demonstrate good homogeneity and SNR for all tissues. Contrasts are in the range of proton density and T_1 contrast, depending on the steady state of the spin system during measurement, see Eq. [3]. The image contrast can be adjusted by changing TR and the flip angle. Prepulses can enable T_2 contrasts. However, gradients have to be ramped down before the prepulses are applied. This is also the case for fat suppression pulses. If two echos are acquired during the measurement, gradients have to be ramped more frequently. Changing the RF phase of the flip angle gives further contrast abilities.

In vivo images in Figs. 5–8 clearly show the expected features of images with very short TE: (a) signal from bones, teeth, ligaments, and tendons, (b) proton density-weighted or T_1-influenced contrast, (c) almost no susceptibility artefacts around air cavities or other magnetic distortions. This can be seen in Fig. 8 (arrow 3), where almost no susceptibility artefacts are visible around the metal screws and bolts used for fixation of the operated anterior cruciate ligament.

On knee and ankle as well as hand images (see Figs. 6–8), ligaments appear bright at TE = 50 and 70 μs. If a second echo is acquired, signal from these tissues has decayed by the time of acquisition and these tissues appear dark in the image.

Imaging of the coil itself, as it can be seen in Fig. 7, may also lead to interesting new applications. Like human

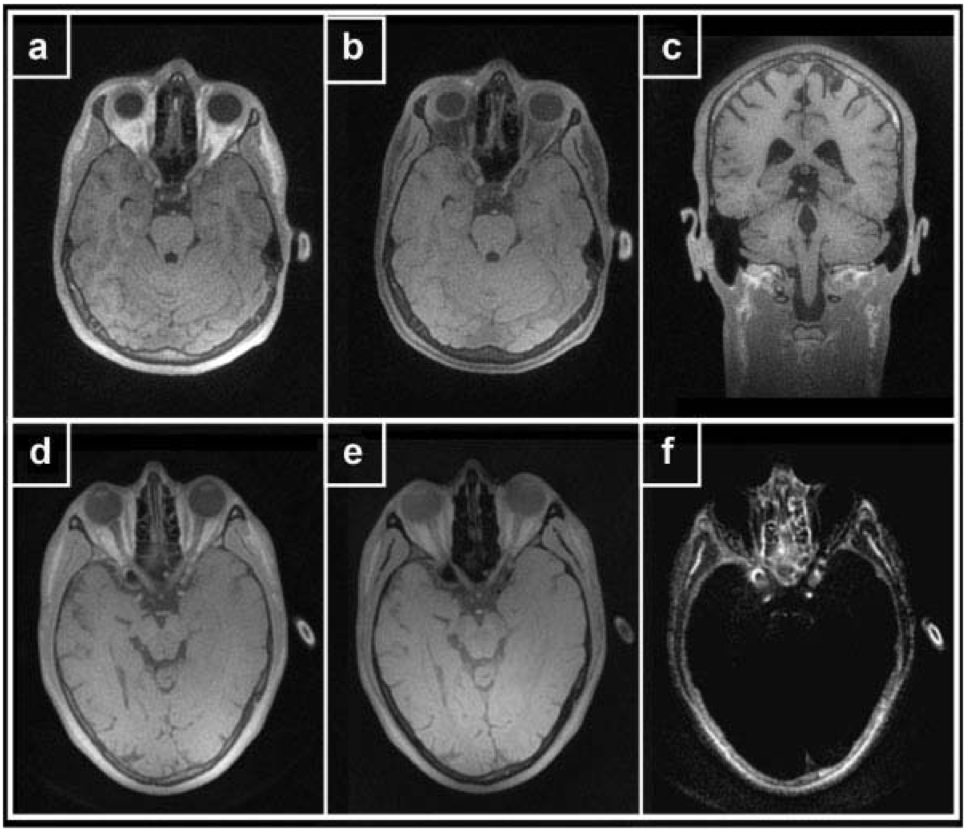

FIG. 5. Images of the head using PETRA with a standard four-channel head coil using $\alpha = 9°$ and $TE_1 = 70\,\mu s$. **a** and **b**: Images without and with fat suppression ($n = 8$), isotropic imaging matrix of 288^3 with a resolution of 1.04 mm and acquisition time $T_A = 3$ min 01′ and $T_A = 4$ min 33′. **c**: Higher resolution image with $T_A = 12$ min 30′, isotropic imaging matrix of 352^3 with a resolution of 0.8 mm. **d** and **e**: Double echo series, isotropic imaging matrix of 256^3 with a resolution of 1.17 mm with acquisition time $T_A = 8$ min 33′ with $TE_2 = 4.6$ ms and the subtraction image in (**f**).

tissue, the coil and its coating attenuate a PET signal. Although signal from coils cannot directly be used as an attenuation map, knowing the exact position of the coil can therefore be included into an algorithm that calculates the attenuation of a known coil. Also, exact localization of a given coil can help to eliminate signal from the coil, which may fold into an image. Localization of the coil may furthermore be used for weighting of different send and receive channels.

PETRA allows fast imaging, as the time consuming Cartesian part only takes a few percent of the total measurement time. Despite the fact that the acquisition time is a bit longer than it is for projection imaging techniques, PETRA is still much faster than pure single point sequences. Compared

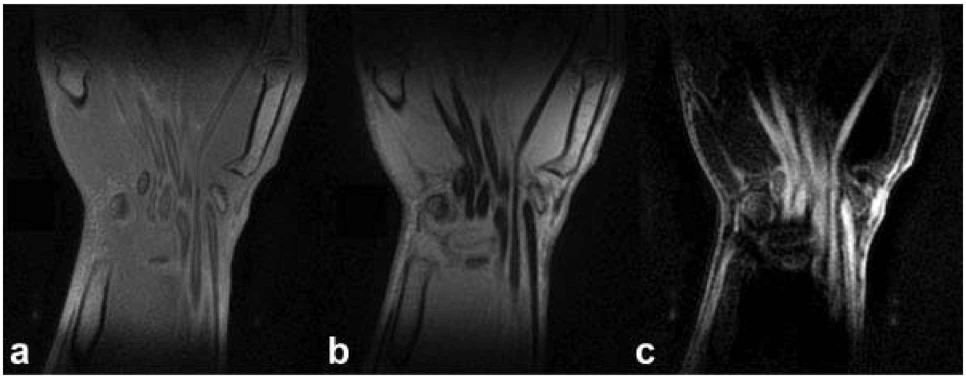

FIG. 6. Images of the wrist using PETRA with a standard eight-channel wrist coil in a coronal image plain. 50,000 radial spokes, $\alpha = 4°$, isotropic imaging matrix of 256^3 with a resolution of 0.78 mm. Spoiling was activated, TR = 8.55 ms, acquisition time $T_A = 10$ min 14′. **a**: shows the first echo at $TE_1 = 50\,\mu s$, (**b**) the second echo at $TE_2 = 4.6$ ms, and (**c**) shows the subtraction of the two echos.

FIG. 7. Subtraction image of the ankle using PETRA with a standard eight-channel ankle coil in a 3D view. 50,000 radial spokes, $\alpha = 9^\circ$, isotropic imaging matrix of 288^3 with a resolution of 1.04 mm. Spoiling was activated, acquisition time $T_A = 7$ min 45′. $TE_1 = 70\,\mu s$ and $TE_2 = 4.6$ ms. Toes are outside of the defined volume of the coil.

to pure projection imaging techniques, encoding times in the outer k-space are equal for PETRA. In our approach, the gap in k-space centre is completely filled with data measured at the absolute shortest encoding time. This might help to increase SNR and stability compared to projection methods. In PETRA, TE can be set to any user-defined value bigger than the minimum TE, that is given by the dead time plus half the pulse duration and is independent of image resolution or available gradient strength. This flexibility in TE in principle enables T_2^* measurements with PETRA.

Like pure projection imaging techniques and single point sequences, PETRA is a 3D only method while UTE enables slice-selective 2D measurements. For PETRA, limitations in flip angle or pulse bandwidth can occur for larger FOV. To avoid any slice selectivity of the pulse for large FOVs, shorter pulses can be used to enable higher excitation bandwidths, but limit the maximum possible flip angle. Otherwise, lower gradients enable longer pulses with higher flip angles, but also lower the readout bandwidth. These limitations also occur in other projection imaging and single-point methods and might be a disadvantage compared to the UTE sequence.

Compared to the standard UTE sequence, PETRA has shorter encoding times over the whole k-space, see Fig. 2. Our approach allows higher resolution and SNR, because more readout points with signal from tissues with short T_2 can be acquired before the signal has decayed. As it can be seen in the simulation in Fig. 3 and the comparison measurement of Fig. 4, this can be an advantage of the PETRA sequence compared to the UTE sequence. PETRA is not sensitive to gradient imperfections, gradient delays, or eddy currents during gradient ramping and has low demands on fast gradient switching and ramping times. This often leads to problems in UTE imaging.

The in vivo results indicate that PETRA might yield clinically relevant applications in orthopedics. MR-PET attenuation correction as well as the application of PETRA in non-proton imaging also merit further investigation.

In conclusion, the hybrid solution of radial projection imaging and single point imaging is feasible. It combines the advantages of both approaches and avoids the problems associated with the UTE approach. The shortest possible TE is achieved, only limited by pulse length and hardware switching times. We have shown that PETRA is able to depict tissue with short T_2 in vitro as well as in vivo. No

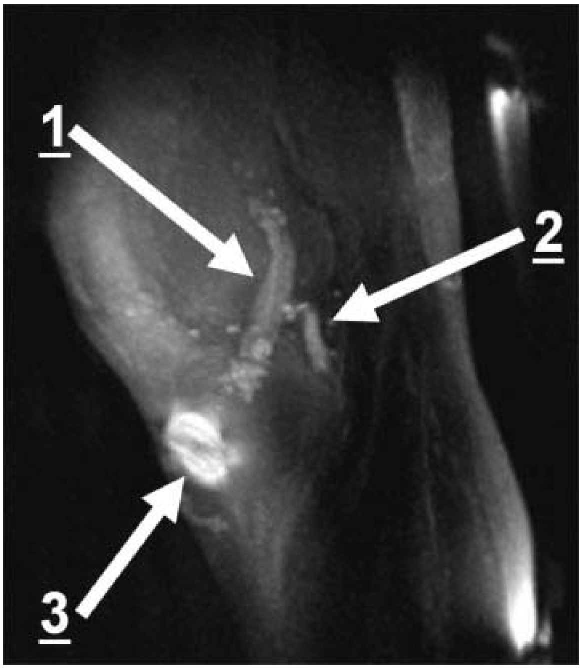

FIG. 8. Sagittal subtraction MIP image of the knee using PETRA with a standard 15-channel knee-coil (MIP thickness = 22 mm). The anterior cruciate ligament was operated after rupture 4 months prior to imaging. Arrows 1 and 2 point to the anterior and posterior cruciate ligament. Arrow 3 marks the bolt that was used to fixate the ligament. 50,000 radial spokes, $\alpha = 4^\circ$, isotropic imaging matrix of 256^3 with a resolution of 0.97 mm. Spoiling was activated, TR = 10 ms, acquisition time $T_A = 8$ min 43′, $TE_1 = 50\,\mu s$ and $TE_2 = 4.6$ ms.

hardware changes or additional hardware requirements are needed. Images with a 1 mm resolution in a 256^3 matrix can be imaged in as fast as 2–4 min for a single echo series. These features might enable or improve orthopedic MR imaging as well as MR-PET attenuation correction.

REFERENCES

1. Gatehouse PD, Thomas RW, Robson MD, Hamilton G, Herlihy AH, Bydder GM. Magnetic resonance imaging of the knee with ultrashort TE pulse sequences. Magn Reson Imaging 2004;22:1061–1067.
2. Filho GH, Du J, Pak BC, Statum S, Znamorowski R, Haghighi P, Bydder G, Chung CB. Quantitative characterization of the Achilles tendon in cadaveric specimens: T_1 and T_2^* measurements using ultrashort-TE MRI at 3 T. Am J Roentgenol 2009;192:W117–W124.
3. Du J, Pak BC, Znamirowski R, Statum S, Takahashi A, Chung CB, Bydder GM. Magic angle effect in magnetic resonance imaging of the Achilles tendon and enthesis. Magn Reson Imaging 2009;27:557–564.
4. Waldman A, Rees JH, Brock CS, Robson MD, Gatehouse PD, Bydder GM. MRI of the brain with ultra-short echo-time pulse sequences. Neuroradiology 2003;45:887–892.
5. Robson MD, Bydder GM. Clinical ultrashort echo time imaging of bone and other connective tissues. NMR Biomed 2006;19:765–780.
6. Robson MD, Gatehouse PD, So PW, Bell JD, Bydder GM. Contrast enhancement of short T_2 tissues using ultrashort TE (UTE) pulse sequences. Clin Radiol 2004;59:720–726.
7. Kuethe DO, Caprihan A, Fukushima E, Waggoner RA. Imaging lungs using inert fluorinated gases. Magn Reson Med 1998;39:85–88.
8. Liu W, Dahnke H, Rahmer J, Jordan EK, Frank JA. Ultrashort T_2^* relaxometry for quantitation of highly concentrated superparamagnetic iron oxide (SPIO) nanoparticle labeled cells. Magn Reson Med 2009;61:761–766.
9. Zhou R, Idiyatullin D, Moeller S, Corum C, Zhang H, Qiaoz H, Zhong J, Garwood M. SWIFT detection of SPIO-labeled stem cells grafted in the myocardium. Magn Reson Med 2010;63:1154–1161.
10. Nielles-Vallespin S, Weber MA, Bock M, Bongers A, Speier P, Combs SE, Wohrle J, Lehmann-Horn F, Essig M, Schad LR. 3D radial projection technique with ultrashort echo times for sodium MRI: clinical applications in human brain and skeletal muscle. Magn Reson Med 2007;57:74–81.
11. Anumula S, Magland J, Wehrli SL, Zhang H, Ong H, Song HK, Wehrli FW. Measurement of phosphorus content in normal and osteomalacic rabbit bone by solid-state 3D radial imaging. Magn Reson Med 2006;56:946–952.
12. Keereman V, Fierens Y, Broux T, De Deene Y, Lonneux M, Vandenberghe S. MRI-based attenuation correction for PET/MRI using ultrashort echo time sequences. J Nucl Med 2010;51:812–818.
13. Brittain JH, Shankaranarayanan A, Ramana V, Shimakawa A, Cunningham CH, Hinks S, Francis R, Turner R, Johnson JW, Nayak KS, Tan S, Pauly JM, Bydder GM. Ultra-short TE imaging with single-digit (8 μs) TE. In proceedings of the 12th annual meeting of ISMRM, Kyoto, Japan, 2004. p. 629.
14. Nauerth A, Gewiese B. SPI—single point FID imaging. In proceedings of SMRM, New York, USA, 1993. p. 1215.
15. Heid O, Deimling M. rapid single Point (RASP) imaging. In Abstracts of the 3rd SMR annual meeting, 1995. p. 684.
16. Balcom BJ, Macgregor RP, Beyea SD, Green DP, Armstrong RL, Bremner TW. Single-point ramped imaging with T_1 enhancement (SPRITE). J Magn Reson A 1996;123:131–134.
17. Heid O. Sensitivity enhanced single point imaging. In Proceedings of SMRM, San Francisco, California, 1998. p. 2186.
18. Halse M, Rioux J, Romanzetti S, Kaffanke J, MacMillan B, Mastikhin I, Shah NJ, Aubanel E, Balcom BJ. Centric scan SPRITE magnetic resonance imaging: optimization of SNR, resolution, and relaxation time mapping. J Magn Reson 2004;169:102–117.
19. Grodzki DM, Deimling M, Heismann B, Fautz HP, Jakob P. Single point sequences with shortest possible TE - GOSPEL. In Proceedings of the 18th annual meeting of ISMRM, Stockholm, Sweden, 2010. p. 2977.
20. Pauly JM, Conolly SM, Nishimura DG, Macovski A. Slice-selective excitation for very short T_2 species. In Proceedings of SMRM, 1989. p. 28.
21. Tyler DJ, Robson MD, Henkelman RM, Young IR, Bydder GM. Magnetic resonance imaging with ultrashort TE (UTE) PULSE sequences: technical considerations. J Magn Reson Imaging 2007;25:279–289.
22. Gatehouse PD, Bydder GM. Magnetic resonance imaging of short T_2 components in tissue. Clin Radiol 2003;58:1–19.
23. Hafner S. Fast imaging in liquids and solids with the Back-projection Low Angle ShoT (BLAST) technique. Magn Reson Imaging 1994;12:1047–1051.
24. Madio DP, Lowe IJ. Ultra-fast imaging using low flip angles and FIDs. Magn Reson Med 1995;34:525–529.
25. Kuethe DO, Caprihan A, Lowe IJ, Madio DP, Gach HM. Transforming NMR data despite missing points. J Magn Reson 1999;139:18–25.
26. Wu Y, Dai G, Ackerman JL, Hrovat MI, Glimcher MJ, Snyder BD, Nazarian A, Chesler DA. Water- and fat-suppressed proton projection MRI (WASPI) of rat femur bone. Magn Reson Med 2007;57:554–567.
27. Wu Y, Hrovat MI, Ackerman JL, Reese TG, Cao H, Ecklund K, Glimcher MJ. Bone matrix imaged in vivo by water- and fat-suppressed proton projection MRI (WASPI) of animal and human subjects. J Magn Reson Imaging 2010;31:954–963.
28. Idiyatullin D, Corum C, Park JY, Garwood M. Fast and quiet MRI using a swept radiofrequency. J Magn Reson 2006;181:342–349.
29. Weiger M, Pruessmann KP, Hennel F. MRI with zero echo time: hard versus sweep pulse excitation. In Proceedings of the 18th annual meeting of ISMRM, Stockholm, Sweden, 2010. p. 695.
30. van Vaals JJ, Brummer ME, Dixon WT, Tuithof HH, Engels H, Nelson RC, Gerety BM, Chezmar JL, den Boer JA. “Keyhole” method for accelerating imaging of contrast agent uptake. J Magn Reson Imaging 1993;3:671–675.
31. Saff EB, Kuijlaars ABJ. Distributing many points on a sphere. Math Intell 1997;19.1:5–11.
32. Sussman MS, Pauly JM, Wright GA. Design of practical T_2-selective RF excitation (TELEX) pulses. Magn Reson Med 1998;40:890–899.
33. Larson PE, Gurney PT, Nayak K, Gold GE, Pauly JM, Nishimura DG. Designing long-T_2 suppression pulses for ultrashort echo time imaging. Magn Reson Med 2006;56:94–103.
34. Larson PE, Conolly SM, Pauly JM, Nishimura DG. Using adiabatic inversion pulses for long-T_2 suppression in ultrashort echo time (UTE) imaging. Magn Reson Med 2007;58:952–961.
35. Du J, Takahashi AM, Bae WC, Chung CB, Bydder GM. Dual inversion recovery, ultrashort echo time (DIR UTE) imaging: creating high contrast for short-T(2) species. Magn Reson Med 2010;63:447–455.
36. Ropele S, Enzinger C, Seifert T, Fazekas F. Measurement of short and ultrashort T_2 components using progressive binomial RF saturation. Magn Reson Med 2006;56:265–271.
37. Rahmer J, Blume U, Bornert P. Selective 3D ultrashort TE imaging: comparison of “dual-echo” acquisition and magnetization preparation for improving short-T_2 contrast. MAGMA 2007;20:83–92.
38. Pipe JG, Menon P. Sampling density compensation in MRI: rationale and an iterative numerical solution. Magn Reson Med 1999;41:179–186.
39. Pipe JG. Reconstructing MR images from undersampled data: data-weighting considerations. Magn Reson Med 2000;43:867–875.
40. Jackson JI, Meyer CH, Nishimura DG, Macovski A. Selection of a convolution function for Fourier inversion using gridding [computerised tomography application]. IEEE Trans Med Imaging 1991;10:473–478.
41. van Metter R, Beutel J, Kundel H. Handbook of medical imaging, Vol. 1: Medical physics and psychophysics. SPIE; Bellingham, Washington, 2000.